Journal of Materials Chemistry A

ROYAL SOCIETY OF CHEMISTRY

PAPER

View Article Online
View Journal

Cite this: DOI: 10.1039/d5ta04992j

Quantifying electrokinetics of $NaCa_{0.6}V_6O_{16}\cdot 3H_2O$ cathode in aqueous zinc-ion batteries with $ZnSO_4$ electrolyte†

Shichen Sun, Boyu Wang and Kevin Huang *

Aqueous zinc-ion batteries (AZIBs) have been actively studied in recent years as a promising solution for next-generation stationary energy storage due to their inherent safety, low cost, and high energy density. However, their practical deployment remains hindered by the limited cycling stability of cathode materials. Overcoming this challenge requires a detailed understanding of cathodic electrokinetics and degradation mechanisms. In this study, we investigate the electrokinetic behavior of a $NaCa_{0.6}V_6O_{16}\cdot 3H_2O$ (NaCaVO) cathode in $ZnSO_4$ electrolyte through a combined application of the galvanostatic intermittent titration technique (GITT) and electrochemical impedance spectroscopy (EIS). For the first time, we quantify the exchange current density (i_0) and interfacial charge-transfer resistance (R_{CT}) of NaCaVO as a function of states of charge (SOCs). The results reveal that the $V^{4+} \rightleftharpoons V^{3+}$ redox reaction exhibits significantly slower kinetics than the $V^{5+} \rightleftharpoons V^{4+}$ counterpart. Further GITT-EIS studies using D_2O–$ZnSO_4$ electrolyte, complemented by X-ray diffraction (XRD) and X-ray photoelectron spectroscopy (XPS), indicate that the sluggish $V^{4+} \rightleftharpoons V^{3+}$ process is predominantly associated with proton insertion. Distribution of Relaxation Time (DRT) analysis correlates the increased interfacial resistance with the intermediate phase formation induced by this proton insertion. The electrokinetic insights obtained in this work fill critical knowledge gaps in AZIB research and provide a foundation for designing more durable and efficient cathode materials in the future.

Received 20th June 2025
Accepted 19th July 2025

DOI: 10.1039/d5ta04992j

rsc.li/materials-a

1. Introduction

Rechargeable aqueous zinc-ion batteries (AZIBs) are an emerging class of electrochemical energy storage devices well-suited for stationary energy storage where cost-effectiveness, safety, and environmental sustainability are important considerations.[1–5] A typical AZIB consists of a high-energy-density zinc-metal anode, a layered or open-framework cathode, and a zinc-ion-conducting aqueous electrolyte – commonly a zinc salt solution.[6–9] With Zn^{2+} and/or H^+ serving as the working ions, the electrochemical reactions at both cathode/electrolyte and anode/electrolyte interfaces are generally reversible, enabling rechargeable operation – a key advantage over conventional non-rechargeable alkaline Zn/MnO_2 batteries.[10–14]

Despite their promise, the commercial development of AZIBs faces serious challenges, particularly due to degradations associated with the cathode and its interfacial interactions with the electrolyte.[15–17] Therefore, the advancement of AZIB technology critically hinges on the development of high-capacity, durable cathode materials, which in turn requires a thorough understanding of cathodic degradation mechanisms.[1,18–21] Additionally, there remains a substantial knowledge gap in the understanding of cathodic kinetics – especially those that govern the ion storage processes at various states of charge (SOCs).

To date, a major effort in aqueous zinc-ion battery (AZIB) research has been focused on engineering a stable zinc-anode/electrolyte interface to suppress the hydrogen evolution reaction (HER) at the zinc anode and mitigate zinc corrosion. Strategies such as surface coatings and electrolyte additives have been widely explored for this purpose. However, many of these additives inadvertently hinder cathodic kinetics, ultimately compromising overall battery performance despite effectively suppressing HER and reducing corrosion.[22,23]

In comparison, cathode-focused research has primarily centered on compositional modifications of MnO_2[−] and V_2O_5[−] based materials to enhance capacity and cycling stability. A notable example is the pre-insertion of alkaline and alkaline-earth metal cations into V_2O_5-based structures.[8,24–29] In these studies, a variety of *in situ* and *ex situ* surface and bulk characterization techniques – such as X-ray diffraction (XRD), X-ray photoelectron spectroscopy (XPS), Electron Microscopy, Fourier Transform Infrared Spectroscopy (FTIR), and X-ray absorption spectroscopy (XAS) – are routinely employed to probe material properties and elucidate underlying reaction mechanisms. In

Department of Mechanical Engineering, University of South Carolina, SC29201, USA. E-mail: huang46@cec.sc.edu

† Electronic supplementary information (ESI) available. See DOI: https://doi.org/10.1039/d5ta04992j

parallel, conventional electrochemical techniques[30] such as Galvanostatic/Potentiostatic Intermittent Titration (GITT/PITT),[31,32] electrochemical impedance spectroscopy (EIS),[33] and cyclic voltammetry (CV)[34,35] are used to study electrochemical behaviors. Despite these efforts, rigorous investigation of cathodic electrokinetics during actual charge and discharge processes remains rare. Furthermore, many early studies only evaluated charge-transfer resistance (R_{CT}) under open-circuit conditions, which do not accurately represent real operating states of AZIBs, thereby limiting their value for mechanistic understanding and battery performance modeling.

In this study, we present a combined GITT and EIS approach to probe cathodic electrokinetics under actual operating conditions. The cathode material of choice is $NaCa_{0.6}V_6O_{16}\cdot 3H_2O$ (NaCaVO), previously identified in our work as a stable and promising candidate for AZIB applications with outstanding cyclability (*e.g.*, 94% capacity retention after 2000 cycles at 2 A g^{-1} and 83% after 10 000 cycles at 5 A g^{-1}).[36] Electrokinetic measurements were conducted using a three-electrode configuration, with NaCaVO as the working electrode (WE), zinc metal as the counter electrode (CE), Ag/AgCl as the reference electrode (RE), and 2 M $ZnSO_4$ as the electrolyte – an industry-relevant formulation. To deconvolute overlapping electrochemical processes and better interpret cathodic behavior, we also apply Distribution of Relaxation Times (DRT) analysis to EIS spectra, correlating observed features with the formation of interfacial secondary phases. Additionally, to investigate the co-intercalation mechanisms of Zn^{2+} and H^+ into the NaCaVO structure, we employ water isotope solvent D_2O in the $ZnSO_4$ electrolyte system to distinguish the contributions of zinc ions from those of protons.

2. Results and discussion

2.1 Electrokinetics quantification using combined GITT-EIS method

The cyclic voltammetry (CV) profiles of the NaCaVO cathode in 2 M H_2O–$ZnSO_4$ electrolyte at scan rates ranging from 0.1 to 1.0 mV s^{-1} are shown in Fig. 1(a). Two distinct pairs of redox peaks, corresponding to the redox transitions of V-oxidation state, are consistently observed across all scan rates. The high-potential redox couple (D_1 at ~0.81–0.82 V and C_1 at ~0.91–0.93 V *vs.* Zn/Zn^{2+}) is assigned to the $V^{5+} \rightleftharpoons V^{4+}$ redox reaction, while the lower-potential couple (D_2 at ~0.56 V and C_2 at ~0.70 V) is related to the $V^{4+} \rightleftharpoons V^{3+}$ reaction.[37–41] With increasing scan rate, both anodic and cathodic peak currents rise systematically, indicating charge-transfer-controlled behavior. However, the lower-potential peaks (D_2/C_2) are consistently broader and exhibit smaller peak currents relative to D_1/C_1, suggesting that the $V^{4+} \rightleftharpoons V^{3+}$ reaction proceeds with slower kinetics and greater polarization than the $V^{5+} \rightleftharpoons V^{4+}$ reaction. Moreover, the potential separation between cathodic and anodic peaks slightly widens with scan rate, particularly for the V^{3+}/V^{4+} redox couple, further indicating that kinetic limitations and sluggish charge transfer dominate at low potentials. Overall, there is no significant change in redox peak position at different scan rates, justifying our use of potential to characterize electrokinetic behaviors of the $V^{5+} \rightleftharpoons V^{4+}$ and $V^{4+} \rightleftharpoons V^{3+}$ redox reactions during the charge and discharge cycles.

Moreover, to investigate the ion diffusion characteristics in the NaCaVO cathode in H_2O–$ZnSO_4$ system, cyclic voltammetry (CV) conducted at varying scan rates (0.1–1.0 mV s^{-1}) was further analyzed by plotting the peak currents corresponding to distinct redox reactions *vs.* square root of scanning rate to determine diffusion coefficient of the electroactive species of a diffusion-controlled redox process using Randles–Ševčík equation:[42,43]

$$I_p = (2.69 \times 10^5) \times n^{3/2} \times A \times D^{1/2} \times C \times v^{1/2} \quad (1)$$

Here I_p is the peak current (A), n is the number of electrons transferred, A is the electrode area (cm^2), D is the diffusion coefficient ($cm^2\ s^{-1}$) of the electroactive species, C is the molar concentration of electroactive species (mol cm^{-3}), and v is the scan rate (V s^{-1}).

Fig. 1(b) shows that a plot of I_p *versus* $v^{1/2}$ of the four redox peaks follow a linear relationship, indicating semi-infinite diffusion as the rate-limiting process. The calculated diffusion

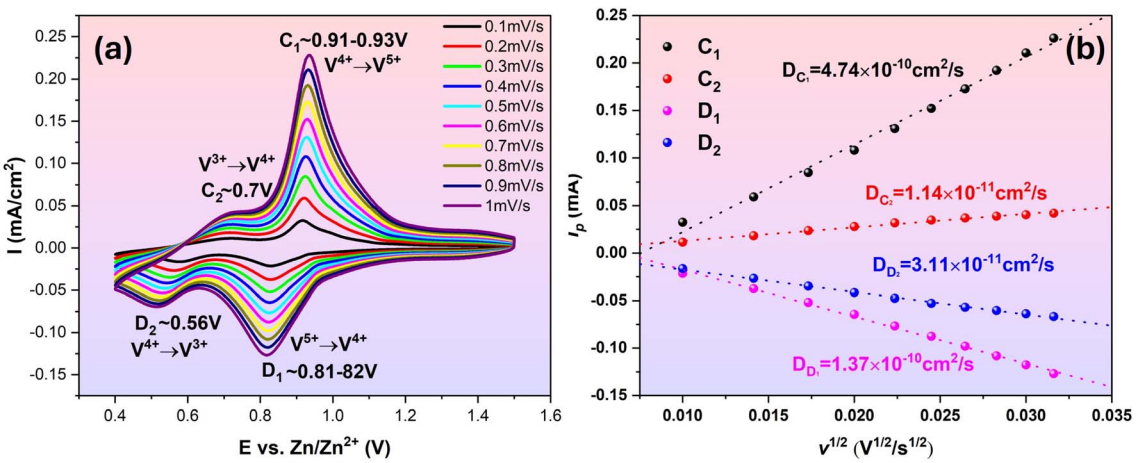

Fig. 1 H_2O–$ZnSO_4$ system: (a) CV and (b) I_p *vs.* $v^{1/2}$ of NaCaVO|2 M $ZnSO_4$|Zn cell scanned at different rates. RE: Ag/AgCl; CE: Zn; WE: NaCaVO.

coefficients related to the four redox peaks are 4.74×10^{-10} and 1.37×10^{-10} cm^2 s^{-1} for C_1 and D_1, respectively, located at the high-potential region and 1.14×10^{-11} and 3.11×10^{-11} cm^2 s^{-1} for C_2 and D_2, respectively, located at the low-potential peaks. The higher D values for the high-potential V^{4+}/V^{5+} redox couple than the V^{3+}/V^{4+} counterpart suggests a facile

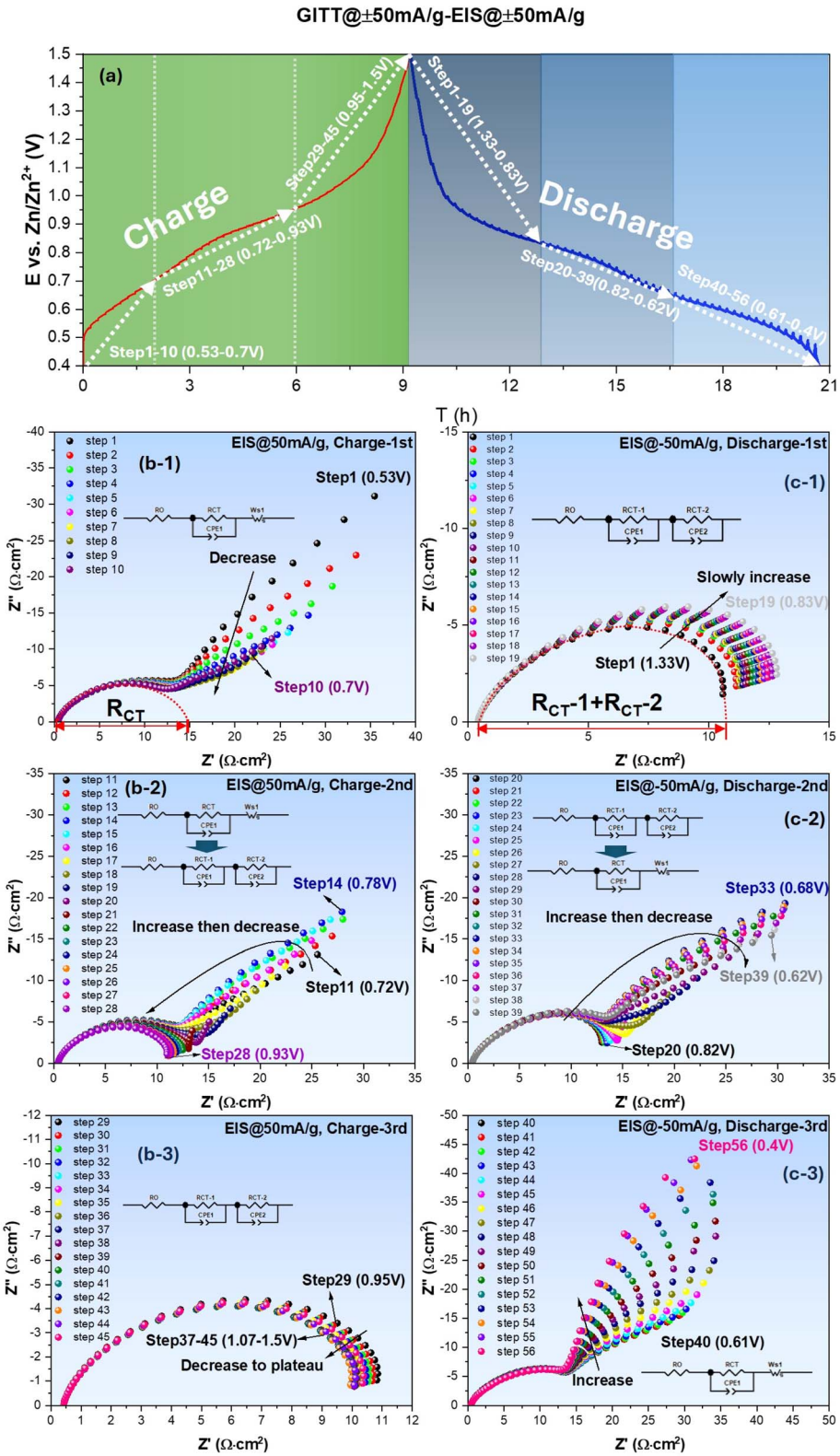

Fig. 2 $ZnSO_4$–H_2O system: (a) *E vs.* time profile collected under ±50 mA g^{-1}; EIS spectra measured with ±50 mA g^{-1} bias during charge (b) and discharge (c) cycles.

kinetics for the former, which will be further discussed in the following sections.

The potential (E) profiles collected by GITT during charge and discharge cycle are shown in Fig. 2(a). As potential E increases and decreases with time during charge and discharge cycle, respectively, pseudo-plateaus regions (quasi-flat regions) show good alignment with the two redox peaks identified in the CV (see Fig. 1(a)). During the charge cycle, the profile exhibits a mid-E pseudo-plateau around 0.85–0.95 V (corresponding to $V^{4+} \rightarrow V^{5+}$ oxidation peak) and a lower pseudo-plateau near 0.60–0.70 V (corresponding to $V^{3+} \rightarrow V^{4+}$ oxidation peak). Similar pseudo-plateaus are also observed during the discharge cycle, corresponding to $V^{5+} \rightarrow V^{4+}$ and $V^{4+} \rightarrow V^{3+}$ reduction peaks, respectively. The greater E changes in lower E region than in higher E region imply higher polarization and sluggish kinetics in the region.

The EIS spectra collected at each GITT step during charge and discharge cycled at $\pm$50 mA g^{-1} (equivalent to $\pm$0.024 mA cm^{-2}) are shown in Fig. 2(b) and (c), respectively, as an example. Each spectrum is measured under different bias currents to obtain R_{CT}= $R_{CT}(i)$ at a specific E (or SOC) created by the preceding galvanic polarization. From Fig. 2(b) collected during the charging cycle, it is evident that EIS spectra feature a charge transfer impedance at high frequencies, followed by low-frequency Warburg impedance (related to semi-infinitive surface diffusion of the active species) over low E range (step 1–10, 0.53–0.70 V). As E increases, the spectra gradually transit to a mixed Warburg (step 11–14, 0.72–0.78 V) and charge-transfer only feature (step 15–28, 0.80–0.93 V) over intermediate E range, and finally to charge-transfer only feature over high E range (step 29–45, 0.95–1.50 V). During the discharging cycle, the above trend remains, *i.e.*, Warburg impedance appears at low E, whereas charge-transfer-only feature appears at high E. Note that the appearance of Warburg impedance at low E range implies diffusion limitation to the active species; we will further correlate it with the formation of an intermediate phase in the following section. The original E *vs.* time profiles and corresponding EIS spectra collected under OCV and other current densities such as 75–125 mA g^{-1} can be found in Fig. S1.† By comparing Fig. 2 and .S1,† it is concluded that the shape of all profiles (two distinct pseudo-plateau regions) remains the same, suggesting that the electrochemical reaction mechanisms remain unchanged by the applied current.

With the equivalent circuit model shown in Fig. 2(b-1), R_{CT} under low E is extracted from the interception length on Z'-axis of the fitted curve (dotted), and for the high E cases, R_{CT} (sum of R_{CT1} and R_{CT2}) is similarly taken using the equivalent circuit model in Fig. 2(c-1). The obtained R_{CT} is then plotted against E and shown in Fig. 3 for both charge and discharge cycle in a current range of 0–125 mA g^{-1}. A clear dependence of R_{CT} on E is observed. In both charge and discharge cycles, the R_{CT}–E profiles can be divided into three stages. Stage-1, the lowest E range (0.40–0.60 V for both charge and discharge), R_{CT} is generally the highest but decreases with E. Stage-2, the intermediate E range (0.68–0.91 V for charge and 0.60–0.83 V for discharge), a maximum is observed. Stage-3, the high E range (>0.91 V for charge and >0.83 V for discharge), a plateau is observed. The minimal R_{CT} appears to occur at a high E close to the $V^{5+} \rightleftharpoons V^{4+}$ as indicated in CV, see Fig. 1(a). In contrast, high R_{CT} appears at lower E range close to the $V^{4+} \rightleftharpoons V^{3+}$. Therefore, we can conclude from Fig. 3 that the $V^{4+} \rightleftharpoons V^{3+}$ redox reaction is more sluggish than the $V^{5+} \rightleftharpoons V^{4+}$ counterpart. This finding could be explained by a greater difficulty in inserting/extracting ions into/from NaCaVO at a deeper SOC. Another reason could be related to the formation of intermediate phase on the surface of NaCaVO cathode due to proton insertion; we will show evidence to support this assertion in a later section. On the other hand, in the higher E and shallow SOC regime, the charge transfer kinetics is facile with low R_{CT}, suggesting a lower presence of the intermediate phase. In addition, the ohmic resistance R_O of all cells studied was roughly ~0.45 Ω cm^2 (see Fig. 2 and S1†), independent of DC bias applied.

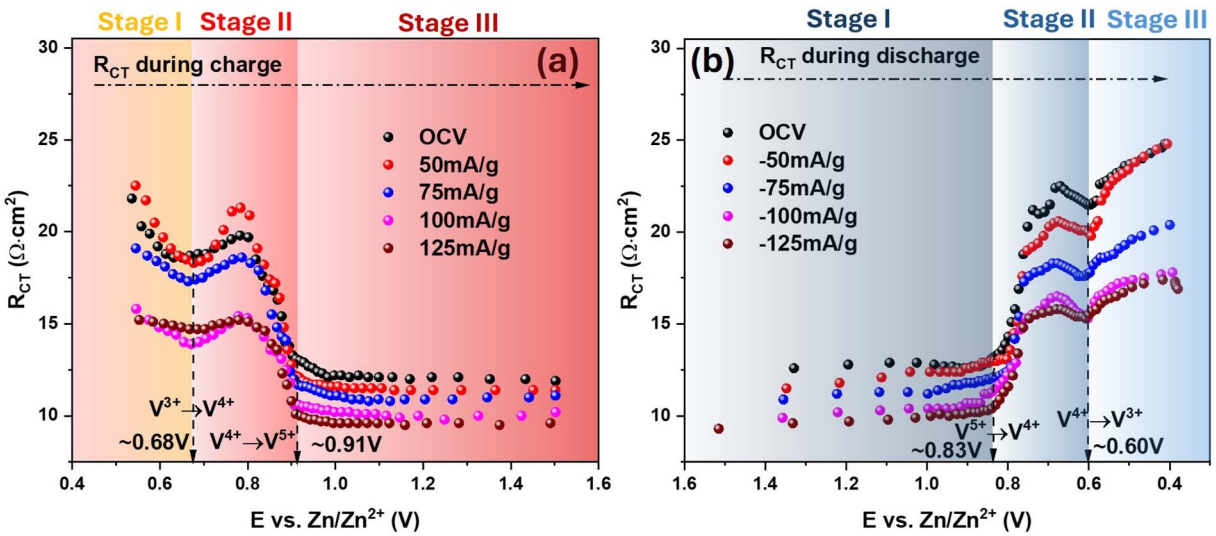

Fig. 3 H_2O–$ZnSO_4$ system: R_{CT} *vs.* E during (a) charge and (b) discharge cycle under different current densities.

The trend of enhanced charge transfer kinetics by the applied current agrees with Butler–Volmer law that predicts higher overpotential drives a lower R_{CT}. The agreement also suggests that the charge transfer kinetics is a rate limiting step of the ion insertion process into NaCaVO. Although the shapes of two R_{CT}–E profiles between charge and discharge cycle are close to a mirror image, the discharge cycle does exhibit a slightly higher R_{CT} than the charge cycle at the same E, indirectly reflecting influence of the intermediate phase formation on charge transfer process.

2.2 Exchange current density (i_0)

With the obtained R_{CT} *vs.* i, we apply the "low-field" approximation of Butler–Volmer equation to extract exchange current density (i_0), a key parameter of electrokinetics, as the current density range applied in this study generally falls into "weak polarization" regime:[44]

$$\eta = (RT/nF) \times i/i_0) \quad (2)$$

where η is the overpotential; i is the applied current density; $n = 1$ is the number of electrons transferred; i_0 is the exchange current density; R and T have their usual meanings. To obtain i-dependent η, we further integrate the experimental $R_{CT} = R_{CT}(i)$ shown in Fig. 4(a) and obtain η–i relationship shown in Fig. 4(b). The selected potentials correspond to the regions where the charge transfer resistance (R_{CT}) reaches a minimum or forms a plateau in the R_{CT} *vs.* E plot (see Fig. 3), specifically at ~0.68 V and ~0.91 V during the charge, and ~0.60 V and ~0.83 V during the discharge, close to those of the redox reactions of $V^{5+} \rightleftharpoons V^{4+}$ and $V^{4+} \rightleftharpoons V^{3+}$. As is shown, a linear relationship is observed with a current density up to 125 mA g^{-1}, implying that the "low-field" approximation is valid.

A comparison of i_0 at different E of the charge and discharge cycle is given in Fig. 4(c); it informs that i_0 is higher at higher E than at lower E. Between the charge and discharge cycle for the same pair of redox reaction, i_0 is higher for the charge cycle than the discharge cycle. Again, these comparisons suggest that the $V^{5+} \rightleftharpoons V^{4+}$ is a more facile redox reaction than the $V^{4+} \rightleftharpoons V^{3+}$ counterpart. We hypothesize that the sluggish $V^{4+} \rightleftharpoons V^{3+}$ redox reaction could be attributed to the intermediate phase formation induced by the H^+ insertion at a deeper SOC. To verify this, we performed a further analysis on EIS spectra with DRT method and replacing of H_2O with D_2O as a solvent for the $ZnSO_4$ electrolyte.

2.3 Analysis of EIS spectra with DRT method

Even though our GITT-EIS method provides E-dependent R_{CT} data under different i, we still do not fully understand the reasons why the kinetics of $V^{5+} \rightleftharpoons V^{4+}$ is faster than $V^{4+} \rightleftharpoons V^{3+}$. We here apply DRT method to facilitate the understanding.[45] Fig. 5 shows an exemplary contour plot of γ-function of DRT analysis over a time domain (τ, relaxation time constant, unit in s) superposed with E (SOC) during a constant polarization at 50 mA g^{-1}, where τ is related to the frequency (f, in Hz) in EIS by:

$$\tau = \frac{1}{2\pi f} \quad (3)$$

By correlating the E *vs.* time profiles with the corresponding DRT contour plots, specific phase formation and deformation processes can be revealed by the emergence or suppression of the $\gamma(\ln\ \tau)$ response in the contour map within defined potential regions. At the peak redox potentials (see Fig. 1(a)), *i.e.* 1.50 to ~0.80 V and ~0.65 to 1.50 V corresponding to the $V^{5+} \rightleftharpoons V^{4+}$ reaction during charging and discharging, respectively, while 0.40 to ~0.80 V and ~0.65 to 0.40 V corresponding to the $V^{4+} \rightleftharpoons V^{3+}$ reaction during charging and discharging, respectively, the DRT plots unveil significant impedance response. At shorter relaxation time (<0.001 s, high frequency), the impedance is generally low in either charge or discharge regimes, implying that the charge transfer process of NaCaVO cathode with $ZnSO_4$ electrolyte is facile. At longer relaxation time (0.1–0.001 s, low frequency), the impedance is high in either charge or discharge regimes, implying possible diffusion limitation. The intermediate phase formed during the discharge process could be responsible for the high impedance at low-frequencies. In fact, the Warburg impedance tails become steeper at higher current densities, see Fig. 2 and S1,† inferring an increasing diffusion resistance. The intermediate phase formed during the discharge cycle could be a reason; we will show the evidence in the following section. For all current densities (OCV, 50, 75 and

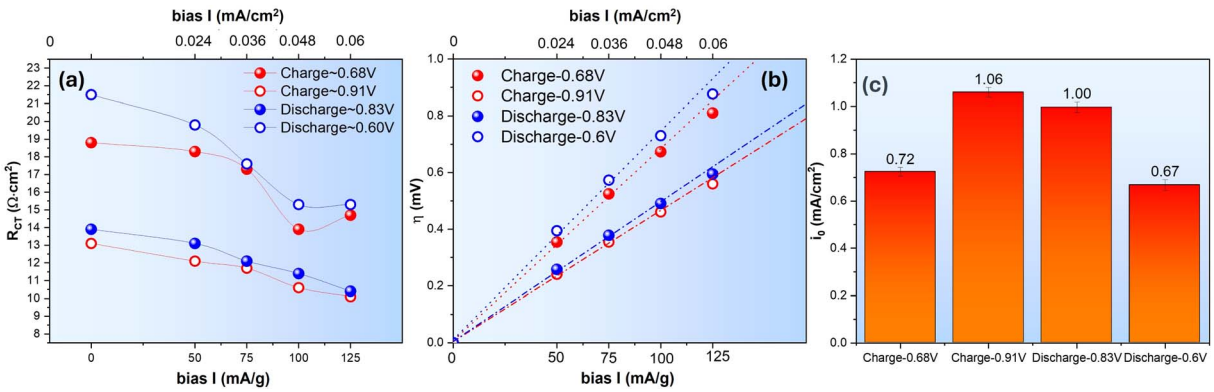

Fig. 4 H_2O–$ZnSO_4$ system. (a) R_{CT} *vs.* i, (b) η *vs.* i and (c) i_0 comparison at 0.68 V and 0.91 V during charge and 0.83 V and 0.6 V during discharge.

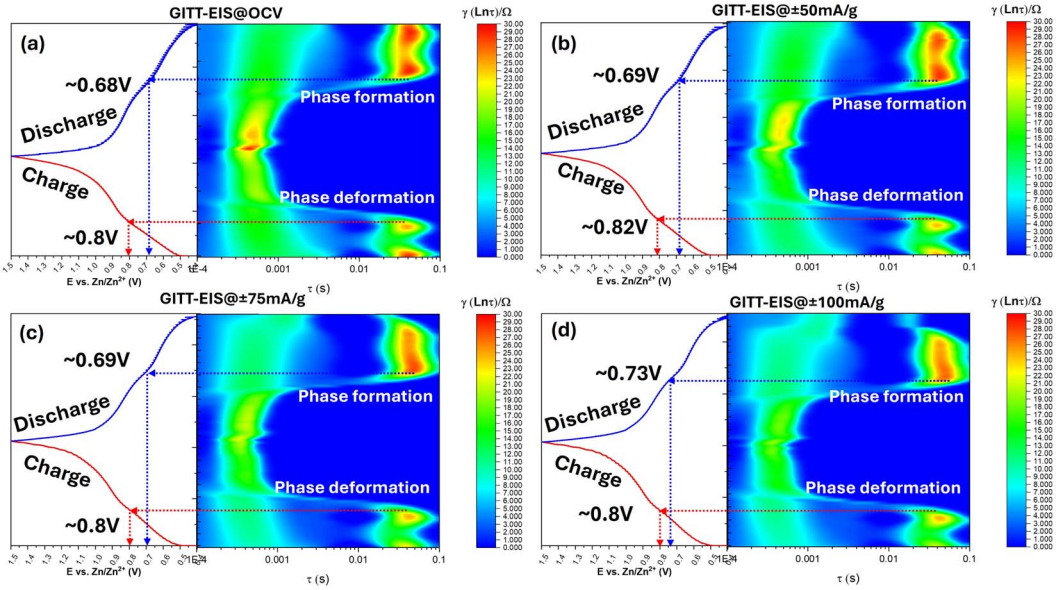

Fig. 5 *E vs.* time profiles (left) and corresponding DRT contour plots (right) derived from EIS of the NaCaVO cathode in H_2O–$ZnSO_4$ electrolyte during charge–discharge cycles under (a) OCV, (b) ±50 mA g^{-1}, (c) ±75 mA g^{-1}, and (d) ±100 mA g^{-1}. The DRT maps reveal phase formation and deformation processes *via* intensity variations in $\gamma(\ln \tau)$ across specific potential ranges.

100 mA g^{-1}), Fig. 5 suggest that this "intermediate phase effect" is reversible upon the charge and discharge cycle.

2.4 Evidence of intermediate phase formation

To identify the composition of the secondary phase, we performed *ex situ* XRD and XPS. Fig. 6 shows XRD patterns of NaCaVO cathode after being cycled under different SOCs. From the main peak of NaCaVO in Fig. 6(a), it is evident that the ion (de)insertion processes are generally reversible during the charge/discharge cycle, exhibiting lattice contraction during the discharge due to strong Zn^{2+}-O^{2-} interactions after Zn^{2+} are inserted and lattice expansion during the charge after Zn^{2+} are extracted. More importantly, Fig. 6(b) indicates that an intermediate phase with a composition of $Zn_4SO_4(OH)_6 \cdot xH_2O$ (herein denoted as Zn-LDH) is detected in NaCaVO only after being cycled at low *E* between 0.40 and 0.80 V (related to $V^{3+} \rightleftharpoons V^{4+}$). The finding of Zn-LDH at low-*E*-cycled NaCaVO provide chemical reason for the slow electrokinetics of $V^{3+} \rightleftharpoons V^{4+}$ and aggravated diffusion impedance. Since it is well known to the AZIB community that Zn-LDH is a product of H^+ insertion into the cathode, it further suggests that H^+ insertion might take place at lower *E*.[46,47] This contrasts with some theoretical calculations suggesting that H^+ insertion takes place mainly at higher *E*.[48–50]

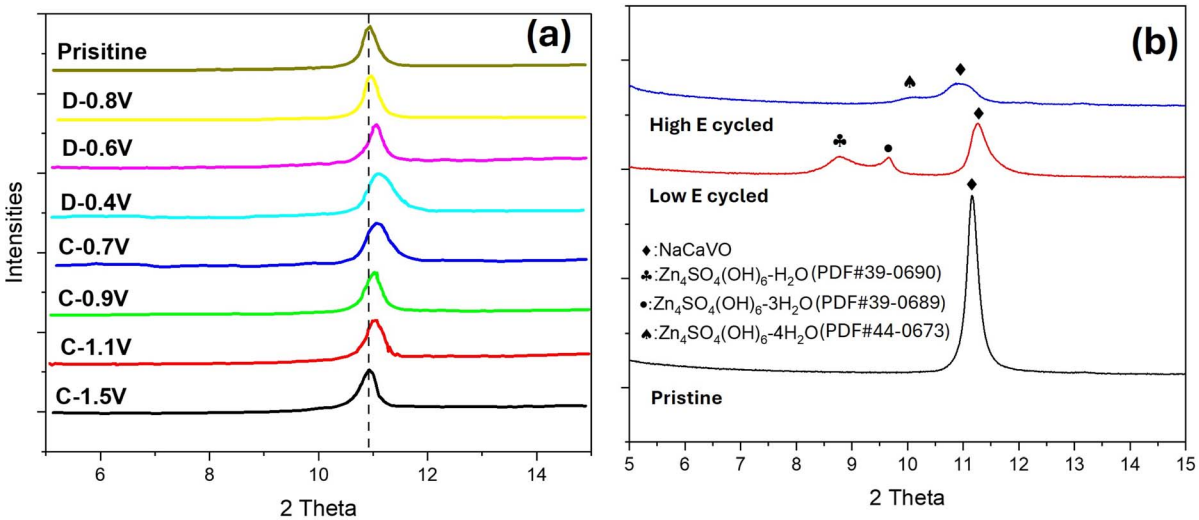

Fig. 6 H_2O–$ZnSO_4$ system. *Ex situ* XRD patterns of NaCaVO cathode after (a) charge and discharge at different SOCs and (b) cycled at low and high E compared with the pristine.

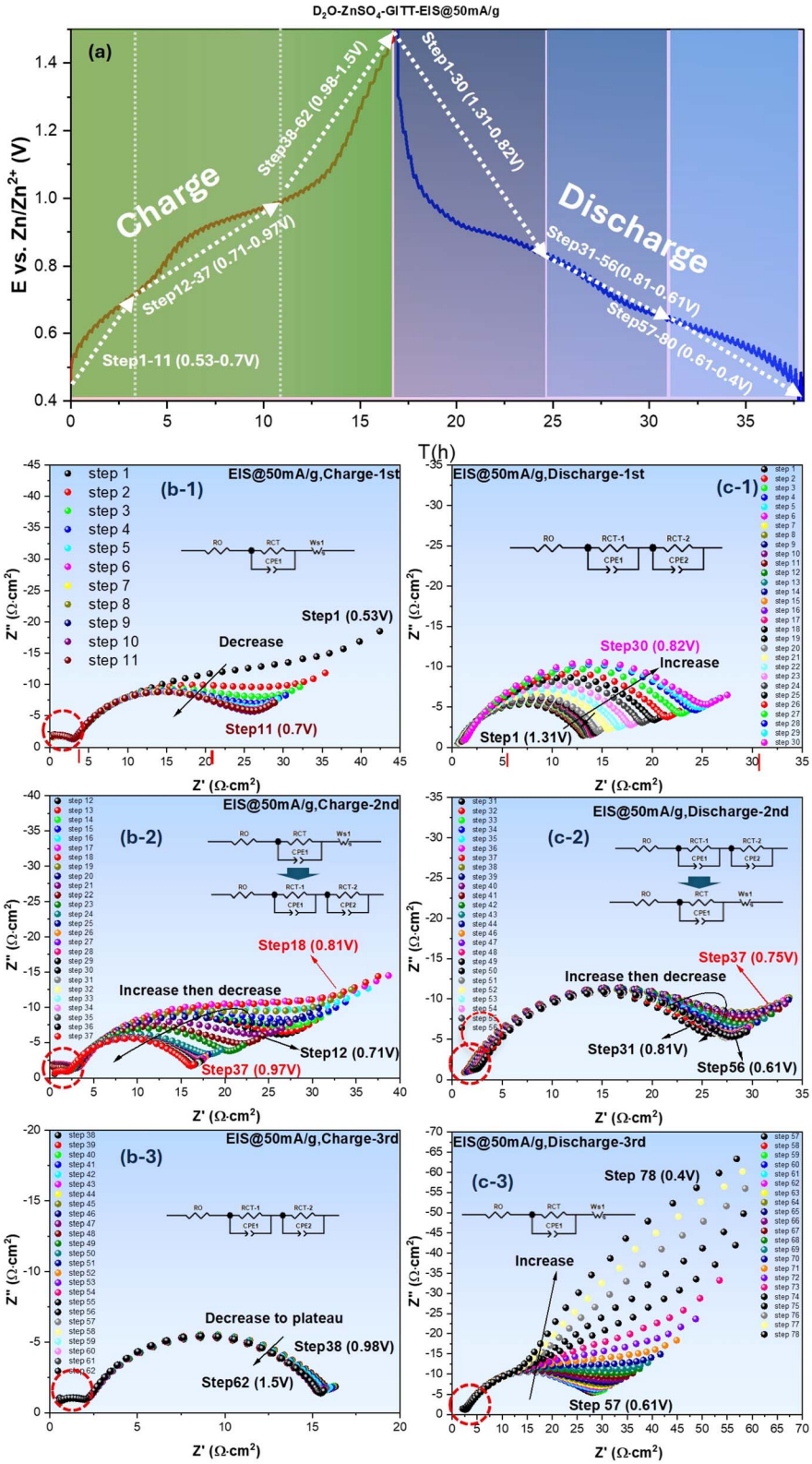

Fig. 7 D_2O–$ZnSO_4$ system: (a) *E vs.* time profile collected under ±50 mA g^{-1}; EIS spectra measured with ±50 mA g^{-1} bias during (b) charge and (c) discharge cycles. Red circles mark the extra semicircle at high frequency range.

The XPS spectra shown in Fig. S4† indicate a weaker V-2p signal in NaCaVO after cycling at low *E* than those of the pristine and cycled at high *E*, suggesting possible blocking effect by the Zn-LDH formed. Furthermore, the ratio of V^{3+}/V^{4+} in NaCaVO becomes significantly higher after cycling at low *E* compared to the pristine (with V^{5+} and trace V^{4+}) and the high-E-

cycled one (with much lower V^{3+}/V^{4+} ratio), which is consistent with our previous results.[36] These XPS results further suggest that the low-E redox reaction is associated with $V^{3+} \rightleftharpoons V^{4+}$ and high-E redox reaction is related to $V^{5+} \rightleftharpoons V^{4+}$.

2.5 Effect of D_2O on electrokinetics

To further verify if the H_2O-derived H^+ insertion into NaCaVO is responsible for the redox reaction of $V^{3+} \rightleftharpoons V^{4+}$, we performed the same GITT-EIS experiment using the same $ZnSO_4$ electrolyte but isotope D_2O as the solvent. Fig. S2† shows the original CV curves of NaCaVO in D_2O–$ZnSO_4$, which is notably different from the H_2O–$ZnSO_4$ case, especially in the low E range (0.5–0.7 V). In particular, the redox peaks associated with the $V^{3+} \rightleftharpoons V^{4+}$ become less pronounced and shifted toward lower E, reflecting the impact of heavier D^+ ions on this redox reaction. The more pronounced broadening and reduced peak current density suggests a retarded reaction kinetics. These observations support the hypothesis that H^+/D^+ impacts on the $V^{3+} \rightleftharpoons V^{4+}$ redox reaction at lower E.

The E-profiles collected from the D_2O–$ZnSO_4$ system under 50 mA g^{-1} by GITT during charge and discharge cycle are shown in Fig. 7 as an example; similar plots at other current densities can be found in Fig. S3.† The two-step pseudo-plateau feature remains, suggesting two active charge transfer processes: $V^{3+} \rightleftharpoons V^{4+}$ and $V^{4+} \rightleftharpoons V^{5+}$. However, a quick glance of EIS spectra indicate that R_{CT} at low E is appreciably higher than the H_2O–$ZnSO_4$ counterpart, inferring that the $V^{3+} \rightleftharpoons V^{4+}$ kinetics has become more sluggish by the slower D^+ (de)insertion process.

A noticeable difference of EIS spectra of the D_2O–$ZnSO_4$ system from H_2O–$ZnSO_4$ system, see Fig. 7(b), is the appearance of a high-frequency semicircle (highlighted by red dotted circles) during the charge cycle. The magnitude of this small semicircle does not seem to change appreciably with SOC. Since D^+ extraction from NaCaVO occurs during the charge cycle, the appeared semicircle (an extra charge transfer process) implies a reduced D^+ extraction kinetics, which leads to a more sluggish $V^{3+} \rightleftharpoons V^{4+}$ redox reaction and increased relaxation time constant. Another notable observation is that the Warburg impedance becomes less pronounced as E increases, the same trend as the H_2O–$ZnSO_4$ system.

For the subsequent discharge cycle, see Fig. 7(c), the EIS collected under high E (Fig. 7(c-1), step 1–19, 1.5–0.83 V) show a much less pronounced, small high-frequency semicircle than that observed during the charge cycle. As E decreases, see Fig. 7(c-2) (steps 20–39, 0.82–0.66 V) and (c-3) (steps 40–56, 0.65–0.4 V), this small high-frequency semicircle appears to increase slightly, while the Warburg impedance becomes more pronounced, like the H_2O–$ZnSO_4$ system. A comparison of EIS spectra *vs.* SOC between the H_2O–$ZnSO_4$ and D_2O–$ZnSO_4$ systems suggests similar charge transfer mechanisms, but the heavier D^+ is more difficult to extract from the cathode, thus increasing the relaxation time constant of the process and depicting itself on the EIS spectrum within the frequency range studied. Since D_2O has the most pronounced impact on R_{CT} at low E, it is reasonable to speculate that H^+/D^+ (de)insertion into the cathode leads to the $V^{3+} \rightleftharpoons V^{4+}$ redox reaction.

To better illustrate how R_{CT} vary with SOC, we plot R_{CT} *vs.* E under different current densities in Fig. 8. In general, the overall trend of each curve resembles Fig. 3 of the H_2O–$ZnSO_4$ system, *i.e.*, they can be divided into three stages, featuring monotonically decreasing, peaking and flattening of R_{CT} with SOC. However, the magnitude of R_{CT} for the $V^{3+} \rightleftharpoons V^{4+}$ is significantly higher (by nearly 2×) in the D_2O–$ZnSO_4$ system than the H_2O–$ZnSO_4$ counterpart, whereas R_{CT} of the $V^{4+} \rightleftharpoons V^{5+}$ is close for the two electrolyte systems. This observation further supports the assertion that it is H^+/D^+ that are mainly responsible for the $V^{3+} \rightleftharpoons V^{4+}$ redox reaction.

The dependence of R_{CT} and η on the applied current density for the D_2O–$ZnSO_4$ system is plotted in Fig. 9(a) and (b), where R_{CT} for the charge and discharge cycle at high E is seen to remain close but notably different at lower E, *i.e.* R_{CT} during the charge is lower than the discharge at a given SOC, which is like the H_2O–$ZnSO_4$ system.

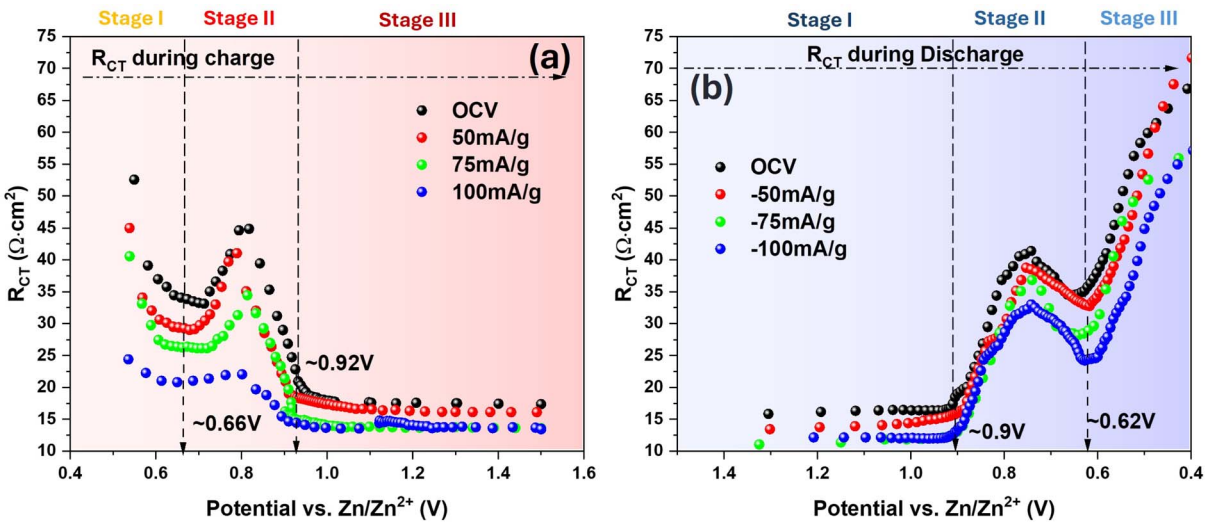

Fig. 8 D_2O–$ZnSO_4$ system: R_{CT} *vs.* E during (a) charge and (b) discharge cycle under different current densities.

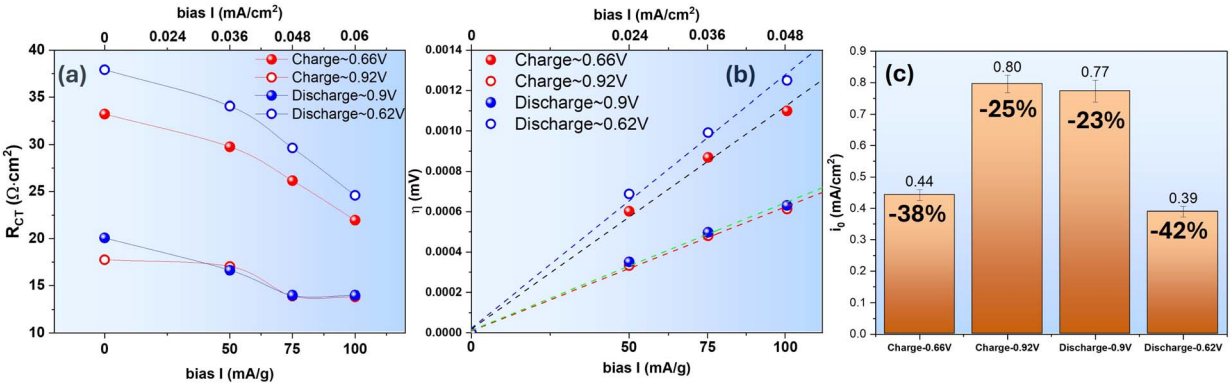

Fig. 9 D_2O–$ZnSO_4$ system: (a) R_{CT} *vs. i*; (b) η *vs. i* and (c) i_0 at 0.66 V and 0.92 V during charge and 0.90 V and 0.62 V during discharge, with relative percentage of decrease compared to the H_2O–$ZnSO_4$ system.

Using the "low-field" approximation, the obtained i_0 of the D_2O–$ZnSO_4$ system is shown in Fig. 9(c). The results indicate a greater decrease in i_0 than the H_2O–$ZnSO_4$ system, *i.e.*, it is −38% and −42% for the charge and discharge cycle, respectively, for the $V^{3+} \rightleftharpoons V^{4+}$ occurring at low *E* and it is −25% and −23% for the charge and discharge cycle, respectively, for the $V^{4+} \rightleftharpoons V^{5+}$ occurring at high E. Such an increased difference could be attributed to the slower D^+ (de)insertion kinetics than H^+.

3. Conclusions

By applying a combined GITT-EIS approach, we quantitatively characterized the electrokinetics of NaCaVO cathode in AZIBs for the first time. Analysis of the charge transfer resistance (R_{CT}) and exchange current density (i_0) reveals that the $V^{3+} \rightleftharpoons V^{4+}$ redox reaction, which occurs at lower potentials during cycling, is intrinsically more sluggish than the $V^{4+} \rightleftharpoons V^{5+}$ counterpart at higher potentials. This difference is likely attributed to two possible factors: (1) a higher energy barrier for charge transfer at a deeper SOC, and/or (2) the formation of an intermediate Zn-LDH phase induced by the H^+ insertion. The possibility of H^+ insertion into the NaCaVO structure is further supported by XRD and XPS analyses, as well as by the observed increase in R_{CT} upon replacing solvent H_2O with D_2O in the electrolyte. Since H^+ insertion into oxide-based cathodes is inevitable, the resultant Zn-LDH formation can also be viewed as an alternative way of Zn-ion storage. Overall, this study provides important fundamental insights into ion storage mechanisms in V_2O_5-based cathodes and offers electrokinetic parameters for future computational modeling of AZIB systems.

4. Experimental methods

4.1 Cathode synthesis and ink preparation

The NaCaVO cathode is synthesized using a hydrothermal method we developed previously.[36] Briefly, VCl_3 and $Ca(NO_3)_2 \cdot 6H_2O$ are mixed in deionized water with the pH adjusted to 7. The solution is then thermally treated at 190 °C for 24 hours in an autoclave, followed by washing and drying the solid precipitates at 60 °C for 12 hours. The synthesized material is characterized using X-ray diffraction (XRD) to confirm phase purity.

NaCaVO cathode ink is prepared by thoroughly mixing 66 wt% NaCaVO with 20 wt% Super-P and 14 wt% polyvinylidene fluoride (PVDF) in *N*-methyl pyrrolidone (NMP) solvent. The resultant slurry is then coated uniformly onto ϕ10 mm stainless steel meshes with ~0.6 mg cm^{-2} active mass loading, followed by vacuum drying at 120 °C for about 12 h and compression under 10 MPa. The aqueous H_2O–$ZnSO_4$ and D_2O–$ZnSO_4$ electrolytes are prepared by dissolving 2 M $ZnSO_4$–$7H_2O$ (Sigma-Aldrich, ACS reagent, 99%) in DI water and D_2O (Sigma-Aldrich, 99.9 atom% D), respectively.

4.2 Electrochemical measurements

In this study, a 3-electrode electrochemical cell is constructed to characterize electrochemical behaviors of the NaCaVO cathode,[51] in which NaCaVO is used as the WE, a zinc metal as CE, an Ag/AgCl as RE, and 2 M $ZnSO_4$ as the electrolyte. During the measurement, Cyclic Voltammetry (CV) is first performed at different scanning rates (mV s^{-1}) to determine the number of redox reactions and their respective potentials. Once the redox potential is determined, we then cycle the NaCaVO–Zn 3-electrode cell 5 times from 1.5 V to 0.4 V *vs.* Zn/Zn^{2+} at 0.2A g^{-1} to fully activate the cathode. We then perform stepwise GITT-EIS measurements within a voltage window of 1.5 V and 0.4 V *vs.* Zn/Zn^{2+} to simulate charge and discharge cycles. Each GITT-EIS run consists of three phases. Phase-1: a ten-minute constant current polarization at 50 mA g^{-1}, either positive (charge) or negative (discharge), is applied to mockup galvanic charge/discharge operation in a battery; this operation creates many potential intervals representing different SOCs (see later Fig. 2(a)). Phase-2: EIS measurements are carried out right after the galvanic interruption under OCV as well as DC bias current in the range of ±50 to ±125 mA g^{-1} in step of ±25 mA g^{-1} within a frequency range of 1 M Hz to 1 Hz with a base AC amplitude of 1 mA. The DC bias current is superimposed on the AC signal. Phase-3: there is a 1-minute resting period under OCV between each bias current. From the measured EIS spectra, R_{CT} under different bias are obtained using equivalent circuits.

The obtained R_{CT}–i relationship is then used to attain overpotential (η)–i through integration, from which i_0 of NaCaVO at a specific potential can be obtained from the "low-field" approximation of Butler–Volmer equation given the low current density range used in this study. In addition, we also use DRT method to help analyze EIS data and facilitate the identification of elementary steps.

To illustrate the phase compositions and the variations of V-oxidation state with SOCs, we employe XRD and XPS, respectively, to examine NaCaVO cycled at high voltage range (1.5–0.75 V at 0.2 A g^{-1} for 50 cycles) and low voltage range (0.75–0.4 V at 0.2 A g^{-1} for 50 cycles). The cycled samples are thoroughly rinsed with DI water before examinations to avoid interference from the electrolyte.

4.3 Materials characterization

The XRD is performed on fresh and post-tested NaCaVO samples using a Rigaku D/MAX-2100 with Cu Kα radiation (λ = 1.5418 Å). The data are recorded from 5 to 80° with an interval of 0.02° and a scan speed of 2° min^{-1}.

The surface oxidation states of the sample are investigated with AXIS Ultra DLD XPS (Kratos Analytical) instrument. The XPS system is equipped with a non-monochromatic Al Kα source (1486.8 eV) operated at 150 W X-ray gun power, a hemispherical analyzer and a load lock chamber for rapid introduction of samples without breaking vacuum. The X-rays were incident at an angle of 45°, with respect to the surface normal. Analysis was performed at a pressure of $\sim 1 \times 10^{-9}$ Torr and high-resolution core level spectra were acquired in the constant analyzer energy mode using a pass energy of 10 eV and a 0.07 eV step size (for survey scans 80 eV pass energy is used with 0.08 eV step size). The XPS experiments were performed by using a low energy electron beam, directed at the sample, for charge neutralization. The Binding energies (BE) of all peaks are corrected in reference to the C ls peak at 285 eV and given with an accuracy of ±0.2 eV. The curve fitting procedure was carried out using the Avantage software.

Data availability

The data supporting this article have been included as part of the ESI.†

Conflicts of interest

There are no conflicts to declare.

Acknowledgements

This research was sponsored by the U.S. Army Research Office (ARO) and was accomplished under Grant Number W911NF-21-1-0308 and the U.S. Air Force Office of Scientific Research under Grant Number FA9550-23-1-0505. The views and conclusions in this document are those of the authors and should not be interpreted as representing the official policies, either expressed or implied, of ARO or AFOSR or the U.S. Government. The U.S. Government is authorized to reproduce and distribute reprints for Government purposes, notwithstanding any copyright notation herein. The XPS facility receives financial support from the Office of the Vice President for Research, University of South Carolina.

References

1 G. Li, L. Sun, S. Zhang, C. Zhang, H. Jin, K. Davey, G. Liang, S. Liu, J. Mao and Z. Guo, *Adv. Funct. Mater.*, 2024, **34**, 2301291.
2 S. W. Gourley, R. Brown, B. D. Adams and D. Higgins, *Joule*, 2023, **7**, 1415–1436.
3 M. Armand and J.-M. Tarascon, *Nature*, 2008, **451**, 652–657.
4 B. Dunn, H. Kamath and J.-M. Tarascon, *Science*, 2011, **334**, 928–935.
5 Z. Yang, J. Zhang, M. C. Kintner-Meyer, X. Lu, D. Choi, J. P. Lemmon and J. Liu, *Chem. Rev.*, 2011, **111**, 3577–3613.
6 C. Xia, J. Guo, P. Li, X. Zhang and H. N. Alshareef, *Angew. Chem.*, 2018, **130**, 4007–4012.
7 K. Zhu, T. Wu, S. Sun, Y. Wen and K. Huang, *ChemElectroChem*, 2020, **7**, 2714–2734.
8 K. Zhu, T. Wu, W. van den Bergh, M. Stefik and K. Huang, *ACS Nano*, 2021, **15**, 10678–10688.
9 Y. Lu, T. Zhu, W. van den Bergh, M. Stefik and K. Huang, *Angew. Chem., Int. Ed.*, 2020, **59**, 17004–17011.
10 K. Zhu, T. Wu, S. Sun, W. van den Bergh, M. Stefik and K. Huang, *Energy Storage Mater.*, 2020, **29**, 60–70.
11 J. J. Ye, P. H. Li, Z. Hou, W. Zhang, W. Zhu, S. Jin and H. Ji, *Angew. Chem.*, 2024, **136**, e202410900.
12 C. Geng, P. Zhang, J.-M. Wu, J. Qin and W. Wen, *ACS Nano*, 2024, **18**, 33119–33130.
13 W. Sun, F. Wang, S. Hou, C. Yang, X. Fan, Z. Ma, T. Gao, F. Han, R. Hu and M. Zhu, *J. Am. Chem. Soc.*, 2017, **139**, 9775–9778.
14 X. Gao, H. Wu, W. Li, Y. Tian, Y. Zhang, H. Wu, L. Yang, G. Zou, H. Hou and X. Ji, *Small*, 2020, **16**, 1905842.
15 B. Zhang, P. Dong, S. Yuan, Y. Zhang, Y. Zhang and Y. Wang, *Chem Bio Eng.*, 2024, **1**, 113–132.
16 D. S. Liu, Z. Zhang, Y. Zhang, M. Ye, S. Huang, S. You, Z. Du, J. He, Z. Wen and Y. Tang, *Angew. Chem., Int. Ed.*, 2023, **62**, e202215385.
17 B. Tang, L. Shan, S. Liang and J. Zhou, *Energy Environ. Sci.*, 2019, **12**, 3288–3304.
18 S. Zuo, X. Xu, S. Ji, Z. Wang, Z. Liu and J. Liu, *Chem.–Eur. J.*, 2021, **27**, 830–860.
19 B. Yong, D. Ma, Y. Wang, H. Mi, C. He and P. Zhang, *Adv. Energy Mater.*, 2020, **10**, 2002354.
20 Y. Lu, T. Zhu, W. van den Bergh, M. Stefik and K. Huang, *Angew. Chem.*, 2020, **132**, 17152–17159.
21 V. Mathew, B. Sambandam, S. Kim, S. Kim, S. Park, S. Lee, M. H. Alfaruqi, V. Soundharrajan, S. Islam and D. Y. Putro, *ACS Energy Lett.*, 2020, **5**, 2376–2400.
22 X. Gao, H. Dong, C. Su, Y. Dai, Y. Liu, I. P. Parkin, C. J. Carmalt and G. J. E. He, *Energy Environ. Sci.*, 2025, **18**, 13–18.

23 X. Li, J. Xiang, L. Qiu, X. Chen, Y. Zhao, Y. Wang, Q. Yue, T. Gao, W. Liu and D. Xiao, *J. Energy Chem.*, 2025, **100**, 770–778.
24 P. He, G. Zhang, X. Liao, M. Yan, X. Xu, Q. An, J. Liu and L. Mai, *Adv. Energy Mater.*, 2018, **8**, 1702463.
25 Y. Yang, Y. Tang, G. Fang, L. Shan, J. Guo, W. Zhang, C. Wang, L. Wang, J. Zhou and S. Liang, *Energy Environ. Sci.*, 2018, **11**, 3157–3162.
26 C. Liu, Z. Neale, J. Zheng, X. Jia, J. Huang, M. Yan, M. Tian, M. Wang, J. Yang and G. Cao, *Energy Environ. Sci.*, 2019, **12**, 2273–2285.
27 C. Xia, J. Guo, P. Li, X. Zhang and H. N. Alshareef, *Angew. Chem., Int. Ed.*, 2018, **130**, 4007–4012.
28 F. Ming, H. Liang, Y. Lei, S. Kandambeth, M. Eddaoudi and H. N. Alshareef, *ACS Energy Lett.*, 2018, **3**, 2602–2609.
29 T. Lv, G. Zhu, S. Dong, Q. Kong, Y. Peng, S. Jiang, G. Zhang, Z. Yang, S. Yang and X. Dong, *Angew. Chem., Int. Ed.*, 2023, **135**, e202216089.
30 Y. Tan, F. An, Y. Liu, S. Li, P. He, N. Zhang, P. Li and X. Qu, *J. Power Sources*, 2021, **492**, 229655.
31 W. Weppner and R. A. J. Huggins, *J. Electrochem. Soc.*, 1977, **124**, 1569.
32 E. Deiss, *Electrochim. Acta*, 2002, **47**, 4027–4034.
33 S.-I. Pyun and J.-S. Bae, *Electrochim. Acta*, 1996, **41**, 919–925.
34 X. Chen, L. Wang, H. Li, F. Cheng and J. Chen, *J. Energy Chem.*, 2019, **38**, 20–25.
35 B. E. J. Conway, *J. Electrochem. Soc.*, 1991, **138**, 1539.
36 K. Zhu, T. Wu and K. Huang, *Adv. Energy Mater.*, 2019, **9**, 1901968.
37 N. Zhang, Y. Dong, M. Jia, X. Bian, Y. Wang, M. Qiu, J. Xu, Y. Liu, L. Jiao and F. Cheng, *ACS Energy Lett.*, 2018, **3**, 1366–1372.
38 M. Yan, P. He, Y. Chen, S. Wang, Q. Wei, K. Zhao, X. Xu, Q. An, Y. Shuang and Y. Shao, *Adv. Mater.*, 2018, **30**, 1703725.
39 S. Deng, Z. Yuan, Z. Tie, C. Wang, L. Song and Z. Niu, *Angew. Chem., Int. Ed.*, 2020, **59**, 22002–22006.
40 J. Kim, S. H. Lee, C. Park, H. S. Kim, J. H. Park, K. Y. Chung and H. Ahn, *Adv. Funct. Mater.*, 2021, **31**, 2100005.
41 J. Ding, Z. Du, B. Li, L. Wang, S. Wang, Y. Gong and S. Yang, *Adv. Mater.*, 2019, **31**, 1904369.
42 A. J. Bard, L. R. Faulkner and H. S. White, *Electrochemical Methods: Fundamentals and Applications*, John Wiley & Sons, 2022.
43 B. He, Y. Ling, Z. Wang, W. Gong, Z. Wang, Y. Liu, T. Zhou, T. Xiong, S. Wang and Y. Wang, *eScience*, 2024, **4**, 100293.
44 T. F. Fuller and J. N. Harb, *Electrochemical Engineering*, John Wiley & Sons, 2018.
45 T. H. Wan, M. Saccoccio, C. Chen and F. Ciucci, *Electrochim. Acta*, 2015, **184**, 483–499.
46 Z. Li, S. Ganapathy, Y. Xu, Z. Zhou, M. Sarilar and M. Wagemaker, *Adv. Energy Mater.*, 2019, **9**, 1900237.
47 A. Macrelli, M. Olivieri, A. Lamperti, V. Russo, B. Bozzini, M. Menegazzo, G. Bussetti, C. S. Casari and A. L. Bassi, *Electrochim. Acta*, 2023, **442**, 141909.
48 M. Liu, Z. Li and Y. Zhang, *J. Electroanal. Chem.*, 2023, **942**, 117539.
49 F. Gong, Y. Feng, Y.-H. Fang, Y.-K. Hsu and Y.-C. Chen, *ACS Appl. Mater. Interfaces*, 2023, **15**, 18808–18818.
50 D. Zhang, J. Cao, Y. Yue, T. Pakornchote, T. Bovornratanaraks, J. Han, X. Zhang, J. Qin and Y. Huang, *ACS Appl. Mater. Interfaces*, 2021, **13**, 38416–38424.
51 S. Sun, A. Billings, B. Wang and K. Huang, *ACS Electrochem.*, 2024, **1**, 195–204.